https://doi.org/10.5194/se-2019-205
Preprint. Discussion started: 10 January 2020

Solid Earth Discussions

Bromine speciation and partitioning in slab-derived fluids and melts: Implications for halogens recycling in subduction zones

Marion Louvel[1,2], Carmen Sanchez-Valle[2], Wim J. Malfait[3], Gleb S. Pokrovski[4], Camelia N. Borca[5] and Daniel Grolimund[5]

[1]School of Earth Sciences, Bristol University, UK- BS81RJ, Bristol, United-Kingdom
[2]Institute for Mineralogy, WW-Universität Münster, D-48149, Münster, Germany
[3]Swiss Federal Laboratories for Materials Science and Technology EMPA, CH-8600, Dubendorf, Switzerland
[4]Groupe Métallogénie Expérimentale, Géosciences Environnement Toulouse (GET), OMP-CNRS-IRD-University of Toulouse, 14 Avenue Edouard Belin 31400 Toulouse, France
[5]Swiss Light Source, Paul Scherrer Institute, CH-5232, Villigen, Switzerland
Correspondence to: Marion Louvel (louvel@uni-muenster.de)

Abstract. Understanding the behavior of halogens (Cl, Br, and I) in subduction zones is critical to constrain the recycling of trace elements and metals, and to quantify the halogen fluxes to the atmosphere *via* volcanic degassing. Here, the partitioning of bromine between coexisting aqueous fluids and hydrous granitic melts and its speciation in slab-derived fluids have been investigated *in situ* up to 840 °C and 2.2 GPa by X-ray fluorescence (SXRF) and absorption (XANES and EXAFS) spectroscopy in hydrothermal diamond-anvil cells. The partition coefficients $D^{f/m}_{Br}$ range from 15.3 ±1.0 to 2.0 ±0.1, indicating the preferential uptake of Br by aqueous fluids at all investigated conditions. EXAFS analysis further evidences a gradual evolution of Br speciation from hydrated Br ions $[Br(H_2O)_6]^-$ in slab dehydration fluids to more complex structures invoving both Na ions and water molecules, $[BrNa_x(H_2O)_y]$, in hydrous silicate melts and supercritical fluids released at greather depth (> 200 km). In dense fluids containing 60 wt% dissolved alkali-silicates and in hydrous $Na_2Si_2O_5$ melts (10 wt% H2O), Br is found in a “salt-like” structure involving 6 nearest Na ions and several next-nearest O neighbors that are either from water molecules or the tetrahedral silicate network. Bromine (and likely chlorine and iodine) complexation with alkalis is thus an efficient mechanism for the mobilization and transport of halogens by hydrous silicate melts and supercritical fluids, which can carry high amounts of Br, up to the 1000 ppm level. Overall, our results suggest that both shallow dehydration fluids and deeper silicate-bearing fluids efficiently remove halogens from the slab in the sub-arc region, thus controling an efficient recycling of halogens in subduction zones.

Keywords: Bromine, volatile elements, fluxes, speciation, partitioning, slab fluids, halogens, geochemical cycle, subduction zones.

1 Introduction

The fluxes of volatile elements (water, carbon, sulfur, and halogens) in subduction zones play a critical role in the Earth's chemical evolution by controlling the transfer of slab components to the mantle wedge, the volcanic arc and, ultimately, to the atmosphere. Although halogens (F, Cl, Br and I) are rather minor volatiles compared to H_2O and CO_2, their effect on the physical and chemical properties of slab-derived fluids and arc magmas (*e.g.* phase equilibria, viscosity, density), as well as their ability to complex with trace elements and metals makes them key players in the chemical transfer in subduction zones (Zellmer et al., 2015; Barnes et al., 2018). Furthermore, their emission to the troposphere and stratosphere at volcanic arc centres may have significant environmental impact, including 'forced' ozone depletion by Br (Bobrowski et al., 2003; von Glasow et al., 2009; Kutterolf et al., 2013). Constraining halogens cycle at subduction zones is thus crucial to assess their impact on the global atmospheric chemistry and climate.

In the last decade, new developments in quantification technics on pore fluids and rocks as well as in detection methods for halogens species in volcanic gases enabled better estimates of halogen fluxes in subduction zones (Wallace, 2005; Pyle and Mather 2009; John et al., 2011; Kendrick et al., 2013; Kendrick et al., 2015; Chavrit et al., 2016; Barnes et al., 2018). Comparison of the input from the subducted sediments, altered oceanic crust and serpentinized oceanic lithosphere to the output along volcanic arcs points to a strong imbalance between fluorine input and output, suggesting a significant amount of F may be recycled into the mantle (Roberge et al., 2015; Grutzner et al., 2017). On the contrary, Cl, Br and I appear to be efficiently recycled up to the surface, either through shallow loss of pore fluids to the fore-arc region (Br and especially I) or deeper release upon slab dehydration (especially Cl and Br, and to a lesser extent I) (Kendrick et al., 2018). Yet, the poor understanding of the transfer mechanisms and recycling paths of halogens limits the development of integrative numerical models constraining the role of fluids and halogens in the global cycling of elements in subduction zones (Ikemoto and Iwamori, 2014; Kimura et al., 2016). There is for instance virtually no constraint on the amounts of residual halogens that may be stored in the dehydrated slab or lost through hidden hydrothermal activity and passive degassing in the continental crust. Similarly, current knowledge of halogens solubility and speciation in fluids and melts is mostly limited to pressures below 0.3 GPa (equivalent to ~10 km depth), which are relevant to volcanic degassing and ore deposit formation in the shallow crust, but not to slab dehydration or melting beneath arcs at far greater depth (Webster, 1990; Métrich and Rutherford, 1992; Webster, 1992; Bureau et al., 2000; Signorelli and Carroll, 2002; Bureau and Métrich, 2003; Carroll, 2005; Evans et al., 2009; Cadoux et al., 2018). Only recently Bureau et al. (2010, 2016) reported fluid-melt partition coefficients for Br and I in the haplogranite-H_2O system up to 1.7 GPa while Cochain et al. (2015) investigated the speciation of Br in aqueous fluids or haplogranitic melts up to 7.6 GPa. Nevertheless, the effect of fluid chemistry on the speciation and partitioning of halogens at high pressures and temperatures (*P*-*T*) is unknown in subduction zones. To fill this gap, we combine Synchrotron X-ray Fluorescence (SXRF) and X-ray Absorption Spectroscopy (XAS) measurements in a hydrothermal diamond-anvil cell (HDAC) to investigate Br fluid-melt partitioning and speciation in aqueous fluids and hydrous silicate melts that mimic the mobile phases released by the slab at sub-arc depths (Manning, 2004; Frezzotti and Ferrando, 2015). Bromine is employed here as an analog of chlorine amenable to SXRF and XAS studies through the diamond window of the diamond anvil cell due to its higher absorption edge energy, 13.47 keV for bromine K-edge compared to 2.82 keV for chlorine K-edge (Sanchez-Valle, 2013).

https://doi.org/10.5194/se-2019-205
Preprint. Discussion started: 10 January 2020

Furthermore, among the halogens, bromine displays the closest behavior to chlorine in terms of solubility, partitioning and speciation in silicate melts, at least at shallow depths (Bureau et al., 2000, Bureau and Metrich, 2003; Wasik et al., 2005; Bureau et al., 2010; Cadoux et al., 2018). Bromine therefore represents the best analog of Cl for *in-situ* studies at high pressure and high temperature conditions. Our experimental results show gradual changes in the speciation of bromine that reflect changes in fluid composition with depth and constrain the mechanisms controlling the transfer of halogens from the slab to arc magmas.

2. Methods

2.1. Synthesis and characterization of starting materials

The speciation and fluid-melt partitioning experiments were conducted using 3 wt% NaBr aqueous solutions and synthetic sodium disilicate (NS2: $Na_2Si_2O_5$) or haplogranite (Hpg) glasses doped with 1 to 4 wt% Br as starting materials (Table 1). The 3 wt% NaBr aqueous solution was freshly prepared from distilled de-ionized water and analytical grade NaBr powder, sealed in tight containers and refrigerated until the experiments. The NS2 and haplogranite glasses were synthesized in a piston-cylinder apparatus at 1200 °C and 0.5 GPa and 1.5 GPa, respectively, following the method described in Louvel et al. (2013). Briefly, reagent grade powders of SiO_2 and Na_2SiO_3 were employed for the NS2 glasses whereas reagent grade SiO_2, Al_2O_3 and alkali-carbonates, K_2CO_3 and Na_2CO_3, were mixed for the haplogranite glass synthesis. Bromine was added as NaBr powder, and 3.3 wt% H_2O was added as liquid water for the synthesis of the haplogranite glass to ensure complete melting and homogeneization of the sample at run conditions.

Major element composition, Si, Al, K and Na, and glass homogeneity were checked by electron microprobe analyzer (EMPA) using a JEOL JXA-8200 microprobe (Table 1). Electron microprobe analyses of Br are hindered by i) the high ionization potential for the K-lines of Br, which results in low count rates; ii) the peak overlap between the L-lines of Br and the K-lines of Al; and iii) the lack of matrix-matched standards. To overcome these limitations, the concentration of Br in Hpg-Br2 glass sample was determined by Rutherford Backscattering Spectroscopy (RBS). This technique provides absolute elemental concentrations and is particularly appropriated for the quantification of heavy elements in a light matrix as it is the case of Br in silicate glasses (Feldman and Mayer, 1986; Chu and Liu, 1996). The RBS analysis yielded a Br concentration of 0.96 ± 0.04 wt% (Fig. S1 in Supplementary Material), which is identical to the nominal Br concentration within analytical uncertainties. This well-characterized sample was then used as a standard for Br analysis by EMPA and LA-ICPMS in the other glass samples (Table 1 and Supplementary Material).

2.2 Hydrothermal diamond anvil cell experiments

All experiments were conducted in Bassett-type hydrothermal diamond-anvil cells (HDAC, Bassett et al., 1993) widely used for *in-situ* X-ray fluorescence (SXRF) and absorption (XAS) measurements on aqueous fluids and silicate melts up to 1000 °C and about 3 GPa (e.g. Borchert et al., 2009; Louvel et al., 2013, 2014). The HDACs were mounted with a thinner diamond (1.2 mm thick) on the detector side to reduce the X-ray path through the diamonds and widen the collection angle of the XAS analysis (Sanchez-Valle et al., 2004). This configuration allows i) reducing the attenuation of the fluorescence X-rays in the anvil, and ii) decreasing the fluorescence background arising from the Compton/Rayleigh scattering in the thick diamond anvils, hence increasing the overall quality of the analysis. The sample chamber, a 300 µm hole drilled in a 250 µm rhenium gasket compressed between the two diamond anvils, was heated

https://doi.org/10.5194/se-2019-205
Preprint. Discussion started: 10 January 2020

externally with Mo wires wrapped around the tungsten carbide seats supporting the diamond anvils. Temperature was measured to within 2 °C with K-type thermocouples attached to each diamond-anvil, as close as possible to the sample chamber. The temperature gradient between thermocouples and the sample chamber was calibrated for each HDAC prior to experiments using the melting temperature at ambient pressure of S (115.4 °C), $NaNO_3$ (308 °C) and NaCl (800.5 °C). Overall, they remain below 30-35 °C at the highest temperature reached. Pressure was determined from the equation of state of the gold internal pressure standard (Jamieson et al., 1982) whose X-ray diffraction pattern was measured during the experiment.

Partitioning experiments were conducted by loading the sample chamber with a piece of Br-bearing haplogranite glass and either pure H_2O or a 3 wt% NaBr solution (Fig. 1). For the speciation studies by XAS, loadings included either Br aqueous solutions, or a piece of Br-bearing NS2 or haplogranite glass loaded together with distilled de-ionized water. In all runs, a pellet of a mixture of Au $+Al_2O_3$ powders was added to be used for pressure calibration (Louvel et al., 2013; 2014). The volumetric proportions of glass and aqueous fluid in the different loadings were adjusted by adding double-side polished glass pieces of known dimensions (Fig. 1). Upon heating, the haplogranite melt-aqueous fluid system followed the classical phase transitions described in previous studies (Bureau and Keppler, 1999; Louvel et al., 2013), with initial hydrous melting recorded between 550 and 700 °C (Fig. 1B) and complete miscibility reached around 700-850 °C depending on the pressure (Fig. 1C). In contrast, the NS2-H_2O system displays distinct and unusual phase relations in the investigated pressure-temperature range (Fig. 1D-F): the NS2 glass first dissolves completely in the aqueous solution between 150 and 250 °C to produce a single fluid phase, or hydrosilicate liquid, containing 30 to 60 wt%

dissolved Na_2O and SiO_2 solutes (Fig. 1E). Upon further heating between 500 and 750 °C, the fluid unmixes into two phases, a hydrous melt and an aqueous fluid (Fig. 1F). The high temperature immiscibility gap remains open up to the highest temperatures reached with the HDAC (~ 800-900 °C), as previously observed for the haploandesite $Na_2Si_4O_9$-$Na_2(Si,Al)_4O_9$ join and the K_2O-SiO_2-H_2O system (Mysen and Cody, 2004).

The composition of the high pressure fluids (wt% cations dissolved) and melts (wt% H_2O) was determined from available solubility studies (Table 2) as follows. The water content of haplogranite melts at equilibrium with aqueous fluids (Fig. 1B) was calculated from the water solubility data for aluminosilicate melts reported by Mysen and Wheeler (2000) and extended to our experimental conditions. The composition of the aqueous fluids in equilibrium with the haplogranite melts (*i.e.,* total silicates content including SiO_2, Al_2O_3, Na_2O and K_2O) was calculated, by extrapolating up to the *P-T* conditions of our experiments, the solubility data reported in the albite-H_2O system between 0.20 and 0.84 GPa at 600 and 700 °C (Anderson and Burnham, 1983). The composition of the hydrosilicate liquids in the NS2-H_2O system was determined from the initial volumetric proportions of the NS2 glass and the aqueous fluid loaded in the compression chamber. The mass of the glass was calculated from the volume using a density of 2.52(5) g/cm^3 (Yamashita et al., 2008) and that of the fluid determined from the volume left in the compression chamber (Fig. 1D); 4) the amount of water dissolved in the hydrous NS2 melt in equilibrium with the aqueous fluid at 700 °C and 0.4 GPa (Fig. 1F) was calculated from water solubility data in sodium silicate melts reported by Mysen and Cody (2004). The overall error in the calculated bulk compositions is within 10% of the total concentration value.

https://doi.org/10.5194/se-2019-205
Preprint. Discussion started: 10 January 2020

2.3 *In-situ* SXRF/XAS measurements and data analysis

The SXRF and XAS measurements were performed at the MicroXAS beamline (X05-LA) of the Swiss Light Source (SLS, Paul Scherrer Institute, Borca et al., 2009). Measurements at the Br K-edge were conducted with an incident energy of 13.6 keV tuned by a Si(111) double crystal monochromator and focused down to 5 x 8 (V×H) μm^2 size by a set of Rh-coated Kirkpatrick-Baez mirrors. This configuration ensured a photon flux of ~ 2×10^{11} photons per second at the measurements conditions. The intensity of the incident beam was monitored throughout the experiments using an Ar-filled micro-ion-chamber placed between the Kirkpatrick-Baez mirrors and the HDAC. Before measurements, temperature was stabilized for about 30 min after each heating stage to ensure that chemical equilibrium was achieved inside the cell (Louvel et al., 2014). In the case of coexisiting melts and fluid, careful attention was paid that measurements were performed when the melt globule was stationary and bridging both diamonds (Fig. 1F). This configuration ensured that data collection was performed in a pure phase (either fluid or melt) without contamination of the SXRF and XAS signals by the coexisting phase to. SXRF and XAS spectra were collected in fluorescence mode in a forward scattering geometry with an energy dispersive single-element Si-detector (Ketek®, 139 eV resolution at Mn-K_α = 5.89 keV) set at 22° from the incident beam in the horizontal plane (Sanchez-Valle et al., 2003; Louvel et al., 2013; 2014). Angle-dispersive X-ray diffraction spectra were collected on the gold pressure standard before and after XAS/SXRF measurements using a high-resolution CCD camera set in transmission geometry. A microscope equipped with a video camera was used to monitor the compression chamber during the heating and cooling cycles (Fig. 1).

2D-SXRF maps were collected across the sample chamber to qualitatively monitor the distribution of Br between coexisting aqueous fluids and haplogranite melts (Fig. 2). Then, a minimum of three fluorescence spectra was collected in each phase to further determine the Br fluid-melt partition coefficients $D_{Br}^{f/m}$ at each pressure-temperature condition (Table 2). Counting times were set to 100 or 300 s, depending of the intensity of the signal. The fluid-melt partition coefficients $D_{Br}^{f/m}$ at each pressure-tempeature were derived from the integrated intensities of the Br fluorescence emission lines recorded in the fluid and melt, I_f and I_m, after normalization to the incident beam intensity and counting times, and background removal with the Peakfit v4.12 software (SeaSolve Software-USA), following the method described in Louvel et al. (2014). This method relies on the fixed geometry of the HDAC set-up and takes into account the different composition, density (ϱ) and effective transmission (T) of the aqueous fluid and melt to normalize the fluorescence signal and calculates $D_{Br}^{f/m}$ with an uncertainty below 10% according to the equation:

$$\boldsymbol{D}^{f/m} = \frac{\boldsymbol{I}_f}{\boldsymbol{I}_m} \cdot \frac{\boldsymbol{T}_m}{\boldsymbol{T}_f} \cdot \frac{\boldsymbol{\rho}_m}{\boldsymbol{\rho}_f} \qquad (1)$$

Correction parameters are provided in Table 2 and additional details for density and effective transmission calculations are found in Louvel et al. (2014).

XAS measurements were conducted on 3 wt% NaBr aqueous solution, ‘solute-poor’ fluids equilibrated with hydrous haplogranite melt (Fig. 1B), hydrosilicate liquids containing different amounts of dissolved NS2 (Fig. 1E) and hydrous NS2 melt (Fig. 1F). XAS analyses on the haplogranite melt were precluded by the lower Br concentration of these melts (probably < 1000 ppm). For each composition, 3 to 5 XAS spectra were collected with counting times of 1 second per point in the pre-edge region to 3 seconds in the XANES and EXAFS regions. The contribution of Bragg reflections arising from the diamond anvils was avoided in the energy range of interest by changing the orientation of the diamond anvil cell by 0.5 to 1° with respect to the incident X-ray beam direction (Bassett et al., 2000). The edge position was calibrated using a pellet of NaBr powder and no significant drift of the energy was observed during measurements. XAS spectra were also collected at ambient conditions on ~ 200 x 200 μm^2 double-side polished section of the NS2 and haplogranite glasses.

Data reduction was performed using the Athena and Artemis packages (Ravel and Newville, 2005) based on the IFEFFIT program (Newville, 2001). Averaged experimental spectra were normalized to the absorption edge height and background removed using the automatic background subtraction routine AUTOBK included in the Athena software. To minimize the contribution of features at distances below the atom-atom contact distance, the R_{bkg} parameter, which represents the minimum distance for which information is provided by the signal, was set to 1.3 Å. For all spectra, the absorption energy E_0 was set to 13.474 keV, which corresponds to the maximum of the first derivative of the absorption edge. Based on previous studies of Br and Cl speciation in aqueous solutions and silicate glasses (Ayala et al., 2002; D’Angelo et al., 1993; Evans et al., 2008; Ferlat et al., 2001; McKeown et al., 2011; Ramos et al., 2000; Sandland et al., 2004; Stebbins and Du, 2002), our EXAFS analysis includes the Br-O and Br-Na scattering paths as end-members to describe the evolution of the local structure around Br from the high P-T fluids to the hydrous melts and silicate glasses. Although Na cannot be easily distinguished from Al or Si by EXAFS at our spectral resolution, the presence of network cations in the nearest coordination shell of Br is deemed unlikely, as previously shown for Cl by MAS-NMR and XAS studies (Evans et al., 2008; McKeown et al., 2011; Sandland et al., 2004; Stebbins and Du, 2002). The theoretical back-scattering amplitudes F(k), mean free-paths λ(k) and phase-shift functions ϕ(k) for these paths were calculated with the FEFF6.0 *ab initio* code (Mustre de Leon et al., 1991) using an aqueous Br ion $[Br(H_2O)_6]^-$ with mean Br-O distance of 3.37 Å and the NaBr salt crystallographic structure with Br-Na distance of 2.98 Å (Deshpande, 1961; Makino, 1995). Multiple scattering within a linear Br···H-O cluster was also included to model the hydration shell around Br, with the H-O distance fixed to 1.0 Å (Silvestrelli and Parrinello, 1999; Soper and Benmore, 2008). The χ(k) EXAFS function were Fourier filtered over the 1.5 to 6 $Å^{-1}$ k-range for most spectra. For all samples, modelling of the EXAFS oscillations was performed using 4 variables: average coordination number (N), distance to nearest neighbor (R), Debye-Waller factor σ^2, and the energy shift ΔE. The amplitude reduction factor S_0^2 was set to 1 based on previous fits of aqueous NaBr, KBr and $GaBr_3$ solutions (Da Silva et al., 2009; Ferlat et al., 2002). All fits were performed simultaneously with k-weighting of 1, 2 and 3 in order to decrease correlations between N and σ^2, and R and ΔE (Pokrovski et al., 2009a,b). The multi-electronic excitations (MEE) at 34 and 90 (± 0.05) eV above the Br K-edge (D'Angelo et al., 1993) were neglected as they did not significantly contribute to the EXAFS spectra. The variation of ΔE values between different fitted samples was less than ± 4 eV, further confirming the validity of the fitting procedure and the accuracy of the derived interatomic distances.

3 RESULTS AND DISCUSSION

3.1 Bromine partition coefficients in the haplogranite-fluid system

https://doi.org/10.5194/se-2019-205
Preprint. Discussion started: 10 January 2020

The distribution of Br between aqueous fluids and silicate melts at high P-T conditions has been constrained by measuring fluid-melt partition coefficients $D_{Br}^{f/m}$ from 592 to 840 °C and 0.2 to 1.7 GPa in four experimental runs. For all investigated conditions, the $D_{Br}^{f/m}$ values are always higher than 1 (Table 2), confirming the preferential partitioning of Br into the fluid phase, which is also qualitatively evident from the *in-situ* Br distribution maps reported in Figure 2. $D_{Br}^{f/m}$ values vary between 2.0 ±0.1 and 15.3 ±1.0, and fall within the range reported in a previous HDAC study by Bureau et al. (2010) at similar *P-T* conditions (Fig. 3). The $D_{Br}^{f/m}$ values are also found to decrease towards unity with increasing *P-T*, as the compositional and structural differences between aqueous fluid and hydrous melt vanish when approaching the critical conditions for the haplogranite-H_2O system (Bureau and Keppler, 1999). Overall, an important finding here is that the $D_{Br}^{f/m}$ values remain relatively small under high *P-T* conditions. This observation suggests that hydrous melts have a capacity comparable to fluids to carry Br, at 100s to 1000s ppm concentrations under high *P-T* conditions and may thus contribute to the efficient transport and recycling of Br to the mantle wedge and volcanic arcs.

At low pressure conditions relevant to fore-arc or crustal processes, our *in-situ* partition coefficients are, however, slightly lower than those obtained from quenched experiments (Fig. 3). For instance, Bureau et al. (2000) and Cadoux et al. (2018) reported average $D_{Br}^{f/m}$ of 17.5 ±0.6 and 20.2 ±1.2 for albitic and rhyodacitic melts at 900 °C and 0.2 GPa, while we found $D_{Br}^{f/m}$ of 4.8 ±0.3 at 800 °C and 0.2 GPa. We also note that the minimum $D_{Br}^{f/m}$ from Cadoux et al. is of 8.6 ±2.2, even closer to our *in-situ* value. These rather small discrepancies may underline issues with pressure determination at low pressure conditions in the HDAC, the quantification of

Br by mass balance techniques in Bureau et al. and Cadoux et al. (i.e, salt precipitates), or artifacts of the quench method resulting in the loss of Br to the aqueous phase upon cooling. Furthermore, slight differences in the melt composition and structure could also result in different Br speciation (Louvel et al., 2020), favoring or not the incorporation of Br in the silicate melt. Under these *P* conditions and similarly low concentration, the available experimental $D_{Br}^{f/m}$ for silicic melts (Bureau et al., 2000; Cadoux et al., 2018; *this study*) are comparable to those reported for Cl. Indeed, fluid-melt partition coefficients from experiments with low Cl concentration (< 1m Cl) range between ~3 and 20 for phonolitic to rhyolitic composition (Chevychelov et al., 2008; Webster and Holloway, 1988; see Dolejs and Zajacz, 2018 for a review), further confirming the similar behavior of Br and Cl under magmatic conditions.

3.2 Speciation of bromine in aqueous fluids and silicate melts

3.2.1 Aqueous solutions and silicate glasses at room conditions

The XANES and EXAFS spectra collected at ambient conditions from the 3 wt%NaBr aqueous solution and Br-bearing silicate glasses are reported respectively in Fig.4 and Fig.5, together with data for a KBr aqueous solution from Ferlat et al. (2002). These spectra were employed to validate the theoretical backscattering amplitude and phase shift functions for Br-O and Br-Na scattering paths used in EXAFS modeling. The XANES spectrum of the 3 wt% NaBr aqueous solution is characterized by an absorption edge at 13.474 keV and a white line that peaks at 13.478 keV (Fig. 4). It displays close similarities to that of the KBr aqueous solution from Ferlat et al. (2002) and overall resembles other alkali bromide aqueous solutions found in the literature (Wallen et al., 1997; Ferlat et al., 2001; Evans et al., 2007). The EXAFS spectra from the KBr and NaBr aqueous solutions are accurately modeled with a hydration shell of 5.7 ±

https://doi.org/10.5194/se-2019-205
Preprint. Discussion started: 10 January 2020

0.8 and 5.9 ± 0.7 water molecules ($N_{Br..H\text{-}O}$) at a Br-O distance of 3.30 ± 0.03 and 3.37 ± 0.04 Å, respectively (Table 3). Note that multiple-scattering paths from the linear Br⋯H-O cluster are needed to accurately reproduce the experimental data; when only Br-O interactions are considered, the model fails to reproduce the amplitude of the EXAFS oscillations unless an unrealistic hydration shell with ~12 H_2O molecules is adopted. The structural parameters fitted for the KBr aqueous solution from Ferlat et al. (2002) are, within errors, similar to those reported by the authors. Together with the EXAFS fits of the NaBr aqueous solution, they confirm that Br speciation in aqueous solution at room conditions is dominated by a six-fold coordinated hydration shell with the H-O bond of the water molecule radially aligned towards the Br ion (Ferlat et al., 2001; Ramos et al., 2000).

EXAFS spectra collected on NS2 and haplogranite glasses at room conditions display distinct oscillations, with a new feature at 2.2 $Å^{-1}$ in both glass samples and amplitudes nearly out of phase after 2 $Å^{-1}$ compared to the NaBr and KBr aqueous solutions (Fig. 5). Different combinations of Br-Na and Br-O scattering paths were tested to constrain the local structural environment of Br in the silicate glasses. Models considering individually either the Br-Na or Br-O paths do not provide a reasonable fit of the EXAFS oscillations and the simultaneous contribution of Br-Na and Br-O bond is required to reproduce the experimental spectra. The EXAFS-derived parameters suggest that Br in NS2 and haplogranite glasses is coordinated to an average of 6 Na cations in the first shell at an average distance of ~2.95 Å and 6 O second neighbors located at ~3.4 Å (Table 3). The fitted Br-Na bond length is consistent, within errors, with theoretical Br-Na distances in crystalline NaBr (2.987 Å, Deshpande, 1961) and is close to that fitted for aluminosilicate glasses in a previous study (Cochain et al., 2015), suggesting Br is incorporated in the silicate glasses in a "salt-like" structure, similar to NaBr. The similarities

https://doi.org/10.5194/se-2019-205
Preprint. Discussion started: 10 January 2020

between the structural parameters fitted for anhydrous NS2 and hydrous haplogranite (3.3 wt% H_2O) glasses also suggest that the nearest environment of Br remains largely anhydrous in glasses containing relatively low water contents and that the O second neighbors may be from the silicate network rather than distinct H_2O or OH groups. Attempts to include the effect of Br⋯H-O bonds in the fitting model by taking into account multiple scattering Br⋯H-O paths instead of Br-O correlations only resulted in a systematic decrease of the fit quality (higher *R*-factor). The sole difference between the two glasses is the presence of a pre-edge feature at ~13.468 keV in the haplogranite glass (Fig. 4). Such features have been attributed to the 1s to 4p electronic transitions in Br (Burattini et al., 1991) and reported in several covalently bonded and/or reduced Br-bearing compounds, including HBr, Br_2, and $CHBr_3$ (D'Angelo et al., 1993; Feiters et al., 2005). While Evans et al. (2007) suggested that this feature could arise from partial Br reduction in the presence of remaining carbon material in the sample from the synthesis, changes in the local site symmetry around Br could also contribute to the development of such feature. Recent HERFD-XAS measurements conducted on silicate glasses however demonstrate that this feature is absent in basaltic and andesitic glasses and hence, specific to the structure of granitic glass compositions (Louvel et al., 2020).

3.2.2 High P-T aqueous fluids and hydrous silicate melts

Bromine K-edge XANES spectra of high *P-T* aqueous fluids (3 wt% NaBr solution, fluids at equilibrium with haplogranite melt and water-dominated fluids containing < 50 wt% dissolved NS2) all share a shape very similar to that of the NaBr aqueous solution at room conditions, suggesting a similar local structure of Br in H_2O-dominated phases at elevated T-P (Fig. 4 and Fig. 5). Differences in the shape of the XANES spectra become more pronounced for the hydrosilicate liquids with >50 wt% dissolved Si and Na and the hydrous NS2 melt (Fig. S2). Although the maximum of the white line remains at 13.478 keV, it broadens and decreases in amplitude compared to the 3 wt% NaBr aqueous solution. Also, the first post-edge resonance is shifted toward either higher (13.504 keV) or lower (13.487 keV) energies compared to the aqueous fluids. We believe these changes may be indicative of the progressive incorporation of Na in the local structure around Br. These modifications of Br coordination environment are also noticeable in the EXAFS oscillations (Fig. 5): while Br-bearing aqueous fluids mostly show a decrease of the amplitude of the oscillations with increasing *P*-*T*, they are shifted to higher distances (*i.e.* from 2.6 to 2.8 $Å^{-1}$ for the first oscillation) for the 60 wt% NS2 fluid. Moreover, the NS2 melt bears closer resemblance to the NS2 and haplogranite glasses, sharing similar oscillations at 2.2 and 3.2 $Å^{-1}$.

The structural parameters derived from the quantitative EXAFS analysis are reported in Table 4. Comparably to room conditions, the EXAFS spectra of 3 wt% NaBr aqueous solution at high pressure-temperature conditions are well reproduced by an octahedral hydration shell including multiple-scattering contributions from the Br···H-O cluster (Fig. 5). Br-O coordination numbers and distances are 6.4 ± 1.1 and 3.40 ± 0.07 Å at 450 °C and 0.6 GPa, indicating the persistence of the 6-fold coordinated hydration shell up to high temperatures. This observation contrasts with results from a number of classical EXAFS studies performed at lower pressures (< 650 bar at 450 ºC) that reported significant reduction in the number of water molecules around Br at supercritical conditions (Wallen et al., 1997; Da Silva et al., 2009). These differences reflect the role of pressure (or fluid density) in stabilizing the hydration shell around Br by increasing the dielectric constant of the solvent with increasing *P* and density (Pan et al., 2013; Sverjensky et al., 2014), as also predicted for other ions such as Li^+ (Jahn and Wunder, 2009) and Ti^{4+} (van Sijl et al., 2010) in molecular dynamics studies. An exception to this trend are the experimental results of Mayanovic et al. (2001), who reported a decrease by >60% of the number of water molecules in the solvation shell of both Br aqua ions and $ZnBr_4^{2-}$ complexes in 1 m $ZnBr_2$ - 6 m NaBr aqueous solution from ambient conditions to 500 ºC and 0.5 GPa. The reason for this discrepancy is unclear at this point and additional studies on the speciation of Br in aqueous electrolytes will be necessary to explain the disagreement.

There are no significant changes in Br speciation in the aqueous fluids equilibrated with haplogranitic melts, which contain only few wt% of dissolved silicate components, and in fluids containing up to 30 wt% dissolved NS2 (Fig. 6; Table 4). The first noticeable changes are found for fluids containing 50 wt% dissolved NS2, with a small decrease of the average Br coordination number ($N_{Br\cdots H\text{-}O}$) to ~ 4.7 compared to more dilute fluids (~6.0). While this value stays within errors from the other compositions, the reduction of the hydration shell might define the onset of Br-Na complexation with increasing amount of Na dissolved in the fluid. This hypothesis was tested by introducing a Br-Na contribution in the fitting model for the high temperature data, but this resulted in a decrease of the overall fit quality. The formation of Br-Na complexes and the partial dehydration of Br however becomes evident with further increase of the solute content to 60 wt% dissolved NS2 in the fluid (Table 4). For this composition, the best-fit model is consistent with the presence of ~ 3 Na atoms and 4 to 5 H_2O molecules (or OH groups) in the nearest environment of Br, at 480 °C and 1.5 GPa and 610 ºC and 2.2 GPa. In the NS2 hydrous melt (10 wt% H_2O), the number of Na neighbors further increases to ~ 6 whereas the number of oxygens remains similar to that of the 60 wt% NS2 fluid (~ 3.4). This increase in the number of Na neighbors compared to the 60 wt% NS2-bearing fluid suggests that the nearest environment of Br progressively approaches the local structure observed in the NS2 glass. Yet, the Br local environement remains hydrated, in contrast to the NS2 and haplogranite glasses. Based on results from FTIR and ^{29}Si NMR studies showing that molecular H_2O is favored in aluminosilicate and sodium silicate glasses as the amount of dissolved water increases (Stolper, 1982; Uchino et al., 1992; Xue and Kanzaki, 2004; Behrens and Yamashita, 2008), we suggest that molecular H_2O, rather than OH groups, would be present around Br in the hydrous NS2 melt. Moreover, we cannot exclude that distinct "fluid-like" $Br(H_2O)_6$ and "glass-like" $BrNa_6$ complexes coexist in the hydrous melt as $[yBr(H_2O)_6 + xBrNa_6]$ moieties, as the average signal of these structures could not be distinguished from $[BrNa_y(H_2O)_x]$ clusters by XANES or EXAFS.

4. Implications for the transport and recycling of halogens in subduction zones

The new partitioning and speciation data derived for bromine in the present study provide direct insights on the recycling and transport mechanisms of halogens (Cl, Br and I) in subduction zones. Our results suggest that the mobilization of Br (and likely Cl, Br and I) in subduction zones is affected by the chemistry of the slab-derived mobile phases. These phases, in turn, are essentially controlled by the slab composition and the depth of fluid extraction and hence, by the pressure and temperature conditions (Schmidt and Poli, 1998; Manning, 2004; Schmidt et al., 2004; Hermann et al., 2006; Bebout, 2007; Keppler, 2017). Figure 6 illustrates a gradual transition of Br speciation from hydrated species $[Br(H_2O)_6]^-$ to $[BrNa_x(H_2O)_y]$ clusters with various stoichiometries (or mixture of $[Br(H_2O)_6]$ and $BrNa_6$ moieties) as the fluid composition evolves from diluted aqueous fluids such as those released by continuous metamorphic dehydration of the slab (< 15 wt% dissolved solutes, Manning, 2004; Rustioni et al., 2019) to Si/Na-rich supercritical fluids that form owing to enhanced solubility of silicate minerals at depth and/or granitic melts produced by fluid-assisted melting of subducted sediments (Hermann et al., 2006; Skora and Blundy, 2010). The increasing similarities in the local structure of Br in aqueous fluids containing large amounts of dissolved alkali-silica (> 12.5 wt% Na) and the hydrous melts (Fig. 6) is consistent with the progressive decrease in the Br fluid-melt partition coefficients ($D_{Br}^{f/m}$) as with *P*-*T* increase as observed in this study (Fig. 3) and by Bureau et al. (2010). Sodium complexation with Br is thus an efficient mechanism that enables not only aqueous fluids but also hydrosilicate liquids and hydrous melts to carry significant amounts of Br at depth.

General similarities between Cl, Br and I speciation in aqueous solutions and silicate glasses (Evans et al., 2008; McKeown et al., 2011,2015; Shermann et al., 2010) suggest that the speciation and partitioning trends found in our study for Br may extend to Cl and I. Therefore, while pore fluids and early dehydration fluids should release large amounts of halogens to the fore-arc and the mantle wedge (100 – 200 km depth), hydrous slab melts and supercritical fluids play a critical role in recycling the residual halogens dragged by the subducting slabs to greater depths. Such efficient recycling, where most of the Cl and Br subducted is transfered to the mantle wedge and ultimately returned to the surface through arc magmatism, is further supported by recent quantification of halogens in subducted sediments, serpentinites and altered oceanic crust. Mass balance calculations indeed show a close match between worldwide yearly influx to the mantle wedge, ~ 13-15 x10^3 kt/yr Cl and 5-70 kt/yr Br, and calculated outflux as HCl and HBr at volcanic arcs, ~ 3-22 x10^3 kt/yr Cl and 5-15 kt/yr Br. (Barnes et al., 2018; Chavrit et al., 2016; Kendrick et al., 2013; Pyle and Mather, 2009). In comparison, iodine degassing at volcanic arcs is less well constrained, making it more difficult to assess its fate in the subduction factory (e.g., Bureau et al., 2016). The small imbalances remaining between Cl and Br input and output fluxes may arise from difficulties in quantifying halogens loss to the fore-arc and crustal hydrothermal systems. Recent reports of halogens enrichment in oceanic islands basalts also point out to the subduction of a noticeable fraction of F, Cl, Br and I to greater depth, to an extent that is still to be quantified (Barnes et al., 2018; Hanyu et al., 2019; Kendrick et al., 2017).

5. Conclusions

In-situ SXRF and XAS have been applied to quantify Br fluid-melt partition coefficients and speciation in aqueous fluids, hydrosilicate liquids and hydrous melts up to 840 °C and 2.2 GPa.Above all, our experimental results demonstrate how changes in speciation, from hydrated ions in aqueous fluids to 'salt-like' structures in hydrous melts, may facilitate the uptake of high amounts of Cl, Br and probably I by subduction zone fluids, regardless of their composition. Significant efforts are however still needed to accurately quantify halogen's cycling from the surface to the deep Earth and back. Especially, new experiments investigating the solubility of halogens in subduction zone fluids and the capacity of high-pressure minerals (e.g., micas, Ti-clinohumite, apatite, nominally anhydrous minerals but also carbonates) to incorporate these elements are still necessary to evaluated the amounts that may be returned to the volcanic arc or retained in the slab.

Acknowledgements: We would like to thank M. Doebeli and J. H. Seo for conducting the RBS and LA-ICPMS analysis, respectively. The Paul Scherrer Institute (PSI) and the Swiss Light Source (SLS) are acknowledged for providing beamtime for the experiments. This work was supported by the Swiss National Science Foundation (grants 200021-120575 and 200020-132208 to CSV) and by the Swiss Academy of Sciences (SATW) and the Ministères des Affaires étrangères et européennes (MAEE) et de l'Enseignement Supérieur et de la Recherche (MESR) through the Partenariat Hubert Curien (PHC).

References

Anderson, G. M. and Burnham, C. W., 1983. Feldspar solubility and the transport of aluminum under metamorphic conditions. Am. J. Sci. 283, 283-297.

Aranovich, L.Y. and Newton, R.C., 1996. H_2O activity in concentrated NaCl solutions at high pressures and temperatures measured by the brucite-periclase equilibrium. Contrib. Mineral. Petr. 125, 200-212.

Ayala, R., Martinez, J. M., Pappalardo, R. R., Saint-Martin, H., Ortega-Blake I. and Sanchez-Marcos, E., 2002. Development of first-principles interaction model potentials. An application to the study of the bromide hydration. J. Chem. Phys. **117**, 10512.

Baasner, A., Hung, I., Kemp, T.F., Dupree, R., Schmidt, B.C. and Webb, S.L., 2014. Constraints on the incorporation mechanism of chlorine in peralkaline and peraluminous Na_2O-CaO-Al_2O_3-SiO_2 glasses. Am. Mineral. 99, 1713-1723.

Balcone-Boissard, H., Villemant, B., and Boudon, G., 2010. Behavior of halogens during the degassing of felsic magmas. Geochem. Geophy. Geosy. **11**.

Barnes, J., Manning, C.E., Scambelluri, M. and Selverstone, J., 2018. The behaviour of halogens during subduction-zone processes. In D.E. Harlov and L. Aranovich (eds.), The Role of Halogens in Terrestrial and Extraterrestrial Geochemical Processes, Springer Geochemistry, 545-590.

Bassett, W. A., Shen, A. H., Bucknum, M., and Chou, I. M., 1993. A New Diamond-Anvil Cell for Hydrothermal Studies to 2.5 GPa and from – 190 °C to 1200 °C. Rev. Sci. Instrum. 64, 2340-2345.

Bassett, W. A., Anderson, A. J., Mayanovic, R. A., and Chou, I.-M., 2000. Hydrothermal diamond anvil cell for XAFS studies of first-row transition elements in aqueous solution up to supercritical conditions. Chem. Geol. **167**, 3-10.

Bebout, G. E., 2007. Metamorphic chemical geodynamics of subduction zones. Earth Planet. Sc. Lett. **260**, 373-393.

Behrens, H. and Yamashita, S., 2008. Water speciation in hydrous sodium tetrasilicate and hexasilicate melts: Constraint from high temperature NIR spectroscopy. Chem. Geol. **256**, 306-315.

Bergstrom, P-A. and Lindgren, J., 1991. An IR study of the hydration of ClO_4^-, NO_3^-, I^-, Br^-, Cl^- and SO_4^{2-} anions in aqueous solution. J. Phys. Chem. 95, 8575-8580.

Bobrowski, N., Honninger, G., Galle, B., and Platt, U., 2003. Detection of bromine monoxide in a volcanic plume. Nature 423, 273-276.

Borca, C. N., Grolimund, D., Willimann, M., Meyer, B., Jefimovs, K., Vila-Comamala, J., and David, C., 2009. The microXASbeamline at the Swiss Light Source: towards nano-scale imaging. J. Phys. Conf. Ser. 186, 1-3.

Borchert, M., Wilke, M., Schmidt, C., and Rickers, K., 2009.Partitioning and equilibration of Rb and Sr between silicate melts and aqueous fluids. Chem. Geol. 259, 39-47.

Burattini, E., D'Angelo, P., Giglio, E. and Pavel, N.V., 1991. EXAFS study of probe molecules in micellar solutions. J. Phys. Chem. 95, 7880-7886.

Bureau, H. and Keppler, H., 1999. Complete miscibility between silicate melts and hydrous fluids in the upper mantle: experimental evidence and geochemical implications. Earth Planet. Sc. Lett. 165, 187-196.

Bureau, H. and Métrich, N., 2003. An experimental study of bromine behaviour in water-saturated silicic melts. Geochim. Cosmochim. Ac. 67, 1689-1697.

Bureau, H., Keppler, H., and Metrich, N., 2000. Volcanic degassing of bromine and iodine: experimental fluid/melt partitioning data and applications to stratospheric chemistry. Earth Planet. Sc. Lett. 183, 51-60.

Bureau, H., Foy, E., Raepsaet, C., Somogyi, A., Munsch, P., Simon, G., and Kubsky, S., 2010. Bromine cycle in subduction zones through in situ Br monitoring in diamond anvil cells. Geochim. Cosmochim. Ac. 74, 3839-3850.

Bureau, H., Auzende A-L., Marocchi, M., Raepsaet, C., Munsch, P., Testemale, D., Mezouar, M., Kubsky, S., Carriere, M., Ricolleau, A. and Fiquet, G., 2016. Modern and past volcanic degassing of iodine. Geochim. Cosmochim. Ac. 173, 114-125.

Cadoux, A., Iacono-Marziano, G., Scaillet, B., Aiuppa, A., Mather, T.A., Pyle, D.M., Deloule, E., Gennaro, E. and Paonita, A., 2018. The role of melt composition on aqueous fluid vs. silicate melt partitioning of bromine in magmas. Earth Planet. Sc. Lett. 498, 450-463.

Carroll, M. R., 2005. Chlorine solubility in evolved alkaline magmas. Annals of Geophysics 48, 619-631.

Carroll, M. R. and Webster, J. D., 1994. Solubilities of sulphur, noble gases, nitrogen, chlorine and fluorine in magmas. Rev. Mineral. Geochem. 30, 231-279.

Chavrit, D., Burgess, R., Sumino, H., Teagle, D.A.H., Droop, G., Shimizu, A. and Ballentine, C.J., 2016. The contribution of the hydrothermal alteration of the ocean crust to the deep halogen and noble gas cycles. Geochim. Cosmochim. Ac. 183, 106-124.

Chevychelov, V.Y., Botcharnikov, R.E. and Holtz, F., 2008. Partitioning of Cl nd F between fluid and hydrous phonolitic melt of Mt. Vesuvius at ~850-1000 °C and 200 MPa. Chem. Geol. 256, 172-184.

Chu, W. K. and Liu, J. R., 1996. Rutherford backscattering spectrometry: Reminiscences and progresses. Mat. Chem. Phys. 46, 183-188.

Cochain, B., Sanloup, C., de Grouchy, C., Crepisson, C., Bureau, H., Leroy, C., Kantor, I., Irifune, T., 2015. Bromine speciation in hydrous silicate melts at high pressure. Chem. Geol. 404, 18-26.

Dalou, C., Mysen, B.O. and Foustoukos, D., 2015. In-situ measurements of fluorine and chlorine speciation and partitioning between melts and aqueous fluids in the Na_2O-Al_2O_3-SiO_2-H_2O system. Am. Mineral. 100, 47-58.

D'angelo, P., Dicicco, A., Filipponi, A., and Pavel, N. V., 1993. Double-electron excitation channels at th Br K-edge of HBr and Br_2. Phys. Rev. A 47, 2055-2063.

Da Silva, C., Proux, O., Hazemann, J. L., James-Smith, J., Testemale, D., and Yamaguchi, T., 2009. X-ray absorption spectroscopy study of solvation and ion-pairing in aqueous gallium bromide solutions at supercritical conditions. J. Mol. Liq. 147, 83-95.

Deshpande, V., 1961. Thermal Expansion of Sodium Fluoride and Sodium Bromide. Acta Crystallogr. 14, 794.

Dolejs, D. and Zajacz, Z., 2018. Halogens in silicic magmas and their hydrothermal systems. In D.E. Harlov and L. Aranovich (eds.), The Role of Halogens in Terrestrial and Extraterrestrial Geochemical Processes, Springer Geochemistry, 431-543.

Evans, K. A., Mavrogenes, J., and Newville, M., 2007. The effect of CO_2 on the speciation of bromine in low-temperature geological solutions: an XANES study. J. Synchrotron Radiat. 14, 219-226.

Evans, K. A., Mavrogenes, J. A., O'Neill, H. S., Keller, N. S., and Jang, L. Y., 2008. A preliminary investigation of chlorine XANES in silicate glasses. Geochem. Geophy. Geosy. 9. Q10003, doi:10.1029/2008GC002157.

Evans, K.A., Gordon, R.A., Mavrogenes, J.A. and Tailby, N., 2009. The effect of CO_2 on the speciation of RbBr in solution at temperatures to 579 °C and pressures to 0.26 GPa. Geochim. Cosmochim. Ac. 73, 2631-2644.

Feldman, L. C. and Mayer, J. W., 1986. Fundamentals of Surface and Thin Film Analysis. Prentice Hall. pp 352.

Ferlat, G., San Miguel, A., Jal, J. F., Soetens, J. C., Bopp, P. A., Daniel, I., Guillot, S., Hazeman, J. L., and Argoud, R., 2001. Hydration of the bromine ion in a supercritical 1 : 1 aqueous electrolyte. Phys. Rev. B 63.

Ferlat, G., San Miguel, A., Jal, J. F., Soetens, J. C., Bopp, P. A., Hazemann, J. L., Testemale, D., and Daniel, I., 2002. The quest for ion pairing in supercritical aqueous electrolytes. J. Mol. Liq. 101, 127-136.

Frezzotti, M.L. and Ferrando, S., 2015. The chemical behavior of fluids released during deep subduction based on fluid inclusions. Am. Mineral. 100, 352-377.

Fulton, J. L., Chen, Y., Heald, S.M. and Balasubramanian, M., 2006. Hydration and contact ion pairing of Ca2+ with Cl- in supercritical aqueous solution. J. Chem. Phys. 125, 094507-1-10.

Fulton, J. L., Schenter, G. K., Baer, M. D., Mundy, C. J., Dang, L. X., and Balasubramanian, M., 2010. Probing the Hydration Structure of Polarizable Halides: A Multi-edge XAFS and Molecular Dynamics Study of the Iodide Anion. J. Phys. Chem. B 114, 12926-12937.

Grutzner, T., Klemme, S., Rohrbach, A., Gervasoni, F. and Berndt, J., 2017. The role of F-clinohumite in volatiles recycling processes in subduction zones. Geology 45, 443-446.

Hanyu, T., Shimizu, K., Ushikubo, T., Kimura, J-I., Chang, Q., Hamada, M., Ito, M., Iwamori, H. and Ishikawa, T., 2019. Tiny droplets of ocean island basalts unveil Earth's deep chlorine cycle. Nat. Commun. 10:60. https://doi.org/10.1038/s41467-018-07955-8.

Heinrich, C. A., Pettke, T., Halter, W. E., Aigner-Torres, M., Audétat, A., Günther, D., Hattendorf, B., Bleiner, D., Guillong, M., and Horn, I., 2003. Quantitative multi-element analysis of minerals, fluid and melt inclusions by laser-ablation inductively-coupled-plasma mass-spectrometry. Geochim. Cosmochim. Ac. 67, 3473-3497.

Hermann, J., Spandler, C., Hack, A. and Korsakov, A.V., 2006. Aqueous fluids and hydrous melts in high-pressure and ultra-high pressure rocks: Implications for element transfer in subduction zones. Lithos 92, 399-417.

Ikemoto, A. and Iwamori, H., 2014. Numerical modeling of trace element transportation in subduction zones : implications for geofluid processes. Earth Planets Space 66:26, 1-10.

Jahn, S. and Wunder, B., 2009. Lithium speciation in aqueous fluids at high P and T studied by ab initio molecular dynamics and consequences for Li-isotope fractionation between minerals and fluids. Geochim. Cosmochim. Ac. 73, 5428-5434.

Jamieson, J. C., Fritz, J. N., and Manghnani, M. H., 1982. Pressure measurement at high temperature in X-ray diffraction studies: gold as a primary standard in High-Pressure Research in Geophysics, pp 27-48. Center for Academic Publishing, Tokyo.

John, T., Scambelluri, M., Frische, M., Barnes, J. D., and Bach, W., 2011. Dehydration of subducting serpentinite: Implications for halogen mobility in subduction zones and the deep halogen cycle. Earth Planet. Sc. Lett. 308, 65-76.

Kendrick, M.A., Honda, M., Pettke, T., Scambelluri, M., Phillips, D. and Giuliani, A., 2013. Subduction zone fluxes of halogens and noble gases in seafloor and forearc serpentinites. Earth Planet. Sc. Lett. 365, 86-96.

Kendrick, M.A., Jackson, M.G., Kent, A.J., Hauri, E.H., Wallace, P.J. and Woodhead, J., 2014. Contrasting behaviours of CO_2, S, H_2O and halogens (F, Cl, Br, and I) in enriched-mantle melts from Pitcairn and Society seamounts. Chem. Geol. 370, 69–81.

Kendrick, M.A., Honda, M. and Vanko, D.A., 2015. Halogens and noble gases in Mathematician Ridge meta-gabbros, NE Pacific: implication for oceanic hyrothermal root zones and global volatile cycles. Contrib. Mineral. Petr. 170:43.

Kendrick, M.A., Hemond, C., Kamenetsky, V.S., Danyushevsky, L., Devey, C.W., Rodemann, T., Jackson, M.G. and Perfit, M.R., 2017. Seawater cycled throughout Earth's mantle in partially serpentinized lithosphere. Nat. Geosci. 10, 222-229.

Kendrick, M.A., Scambelluri, M., Hermann, J. and Padron-Navarta, J.A., 2018. Halogens and noble gases in serpentinites and secondary peroditites: Implications for seawater subduction and the origin of mantle neon. Geochim. Cosmochim. Ac. 235, 285-304.

Keppler, H., 2017. Fluids and trace element transport in subduction zones. Am. Mineral. 102, 5-20.

Kimura, J-I., Gill, J-B., Skora, S., van Keken, P.E. and Kawabata, H., 2016. Origin of geochemical mantle components: Role of subduction filter. Geochem. Geophy. Geosy. 17, 3289-3325.

Louvel, M., Sanchez-Valle, C., Malfait, W.J., Testemale, D. and Hazemann, J-L., 2013. Zr complexation in high pressure fluids and implications for the mobilization of HFSE in subduction zones. Geochim. Cosmochim. Ac. 104, 281-299.

Louvel, M., Sanchez-Valle, C., Malfait, W.J., Testemale, D. and Hazemann, J-L., 2014. Constraints on the mobilization of Zr in magmatic-hydrothermal processes in subduction zones from in situ fluid-melt partitioning experiments. Am. Mineral. 99, 1616-1625.

Louvel, M., Cadoux, A., Brooker, R., Proux, Olivier and Hazemann, J-L., 2020 New insights on Br speciation in volcanic glasses and structural controls on halogens degassing. *Accepted in American Mineralogist.*

Makino, Y., 1995. Correlation between Pseudopotential Radii and Interatomic Distance and Evaluation of Bond Characters for Transition and Lanthanide Elements. J. Alloy. Compd. 227, 18-27.

Manning, C. E., 2004. The chemistry of subduction-zone fluids. Earth Planet. Sc. Lett. 223, 1-16.

Mayanovic, R. A., Anderson, A. J., Bassett, W. A., and Chou, I. M., 2001. Hydrogen bond breaking in aqueous solutions near the critical point. Chem. Phys. Lett. 336, 212-218.

McKeown, D. A., Gan, H., Pegg, I. L., Stolte, W. C., and Demchenko, I. N., 2011. X-ray absorption studies of chlorine valence and local environments in borosilicate waste glasses. J. Nucl. Mater. 408, 236-245.

McKeown, D.A., Muller, I.S. and Pegg, I.L., 2015. Iodine valence and local environments in borosilicate waste glasses using X-ray absorption spectroscopy. J. Nucl. Mater. 456, 182-191.

Mustre de Leon, J., Rehr, J. J., Zabinsky, S. I., and Albers, R. C., 1991. Ab initio curved-wave X-ray-absorption fine structure. Phys. Rev. B 44, 4146-56.

Mysen, B. O. and Cody, G. D., 2004. Solubility and solution mechanism of H_2O in alkali silicate melts and glasses at high pressure and temperature. Geochim. Cosmochim. Ac. 68, 5113-5126.

Mysen, B.O. and Wheeler, K., 2000. Solubility behavior of water in haploandesitic melts at high pressure and high temperature. Am. Mineral. 85, 1128-1142.

Newville, M., 2001. EXAFS analysis using FEFF and FEFFIT. J. Synchrotron Radiat. 8, 96-100.

Pan, D., Spanu, L., Harrison, B., Sverjensky, D.A. and Galli, G., 2013. Dielectric properties of water under extreme conditions and transport of carbonates in the deep Earth. PNAS 110, 6646-6650.

Pokrovski, G. S., Tagirov, B. R., Schott, J., Hazemann, J. L., and Proux, O., 2009a. A new view on gold speciation in sulfur-bearing hydrothermal fluids from in situ X-ray absorption spectroscopy and quantum-chemical modeling. Geochim. Cosmochim. Ac. 73, 5406-5427.

Pokrovski, G. S., Tagirov, B. R., Schott, J., Bazarkina, E. F., Hazermann, J. L., and Proux, O., 2009b. An in situ X-ray absorption spectroscopy study of gold-chloride complexing in hydrothermal fluids. Chem. Geol. 259, 17-29.

Pyle, D. M. and Mather, T. A., 2009. Halogens in igneous processes and their fluxes to the atmosphere and oceans from volcanic activity: A review. Chem. Geol. 263, 110-121.

Ramos, S., Barnes, A. C., Neilson, G. W., Thiaudiere, D., and Lequien, S., 2000. The hydration structure of Br- from anomalous x-ray diffraction. J. Phys.-Condens. Mat. 12, A203-A208.

Ravel, B. and Newville, M., 2005. ATHENA, ARTEMIS, HEPHAESTUS: data analysis for X-ray absorption spectroscopy using IFEFFIT. J. Synchrotron Radiat. 12, 537-541.

Roberge, M., Bureau, H., Bolfan-Cassanova, N., Frost, D.J., Raepsaet, C., Surble,S., Khodja, H., Auzende, A-L. and Fiquet, G., 2015. Is the transition zone a deep reservoir for fluorine? Earth Planet. Sc. Lett. 429, 25-32.

Rustioni, G., Audetat, A. and Keppler, H., 2019. Experimental evidence for fluid-induced melting in subudction zones. Geochem. Perspect. Lett.

Sanchez-Valle, C., 2013. Structure and thermodynamics of subduction zone fluids from spectroscopic studies. Rev. Mineral. Geochem. 76, 265-309.

Sanchez-Valle, C., Martinez, I., Daniel, I., Philippot, P., Bohic, S., and Simionovici, A., 2003. Dissolution of strontianite at high P-T conditions: An in-situ synchrotron X-ray fluorescence study. Am. Mineral. 88, 978-985.

Sanchez-Valle, C., Daniel, I., Martinez, I., Simionovici, A., and Reynard, B., 2004. Progress in quantitative elemental analyses in high P-T fluids using synchrotron x-ray fluorescence (SXRF). J. Phys.-Condens. Mat. 16, S1197-S1206.

Sandland, T. O., Du, L. S., Stebbins, F., and Webster, J. D., 2004. Structure of Cl-containing silicate and aluminosilicate glasses: A ^{35}Cl MAS-NMR study. Geochim. Cosmochim. Ac. 68, 5059-5069.

Sherman, D.M., 2010. Metal complexation and ion association in hydrothermal fluids: insights from quantum chemistry and molecular dynamics. Geofluids 10, 41-57.

Signorelli, S. and Carroll, M. R., 2002. Experimental study of Cl solubility in hydrous alkaline melts: constraints on the theoretical maximum amount of Cl in trachytic and phonolitic melts. Contrib. Mineral. Petr. 143, 209-218.

Silvestrelli, P. L. and Parrinello, M., 1999. Structural, electronic, and bonding properties of liquid water from first principles. J. Chem. Phys. 111, 3572-3580.

Skora, S. and Blundy, J., 2010. High-pressure hydrous phase relations of radiolarian clay and implications for the involvement of subducted sediment in arc magmatism. J. Pet. 51, 2211-2243.

Soper, A. K. and Benmore, C. J., 2008. Quantum Differences between Heavy and Light Water. Phys. Rev. Lett. 101, 065502-1-4.

Stebbins, J. F. and Du, L. S., 2002. Chloride ion sites in silicate and aluminosilicate glasses: A preliminary study by Cl-35 solid-state NMR. Am. Mineral. 87, 359-363.

Stolper, E., 1982. Water in silicate glasses: An infrared spectroscopic study. Contrib. Mineral. Petr. 81, 1-17.

Sverjensky, D.A., Harrison, B. and Azzolini, D., 2014. Water in the deep Earth : The dielectric constant and the solubilities of quartz and corundum to 60 kb and 1200 C. Geochim. Cosmochim. Ac. 129, 125-145.

Uchino, T., Sakka, T., Ogata, Y., and Iwasaki, M., 1992. Mechanism of hydration of sodium-silicate glass in a steam environment - Si^{29} NMR and ab initio molecular-orbital studies. Journal of Physical Chemistry 96, 7308-7315.van Sijl, J., Allan, N. L., Davies, G. R., and van Westrenen, W., 2010.

Titanium in subduction zone fluids: First insights from ab initio molecular metadynamics simulations. Geochim. Cosmochim. Acta 74, 2797-2810.

van Sijl, J., Allan, N. L., Davies, G. R., and van Westrenen, W., 2010. Titanium in subduction zone fluids: First insights from ab initio molecular metadynamics simulations. Geochim. Cosmochim. Acta 74, 2797-2810.

Von Glasow, R., Bobrovski, N. and Kern, C., 2009. The effects of volcanic eruptions on atmospheric chemistry. Chem. Geol. 263, 131-142.

Wallace, P. J., 2005. Volatiles in subduction zone magmas: concentrations and fluxes based on melt inclusion and volcanic gas data. J. Volcanol. Geoth. Res. 140, 217-240.

Wallen, S. L., Palmer, B. J., Pfund, D. M., Fulton, J. L., Newville, M., Ma, Y. J., and Stern, E. A., 1997. Hydration of bromide ion in supercritical water: An X-ray absorption fine structure and molecular dynamics study. J. Phys. Chem. A 101, 9632-9640.

Wasik, A., Dingwell, D.B., Courtial, P. and Hess, K., 2005. Viscosity and chemical diffusion of halogens in silicate melts: implications for volcanic degassing. Eos Trans. AGU 86 (52) Fall Meet. Suppl., Abstract V21E-0667.

Webster, J. D., 1990. Partitioning of F between H_2O and CO_2 fluids and topaz rhyolite melt - Implications for mineralizing magmatic-hydrothermal fluids in F-rich granitic systems. Contrib. Mineral. Petr. 104, 424-438.

Webster, J. D., 1992. Water Solubility and Chlorine Partitioning in Cl-Rich Granitic Systems - Effects of Melt Composition at 2 kbar and 800 °C. Geochim. Cosmochim. Ac. 56, 679-687.

Webster, J. D. and Holloway, J. R., 1988. Experimental constrains on the partitioning of Cl between Topaz Rhyolite melt and H_2O and H_2O+CO_2 fluids. New Implications for granitic differentiation and ore deposition. Geochim. Cosmochim. Ac. 52, 2091-2105.

Webster, J. D. and De Vivo, B., 2002. Experimental and modeled solubilities of chlorine in aluminosilicate melts, consequences of magma evolution, and implications for exsolution of hydrous chloride melt at Mt. Somma-Vesuvius. Am. Mineral. 87, 1046-1061.

Webster, J.D., Kinzler, R.J. and Mathez, E.A., 1999. Chloride and water solubility in basalt and andesite melts and implications for magmatic degassing. Geochim. Cosmochim. Ac. 63, 729-738.

Webster, J. D., Sintoni, M. F., and De Vivo, B., 2009. The partitioning behavior of Cl, S, and H_2O in aqueous vapor-± saline-liquid saturated phonolitic and trachytic melts at 200 MPa. Chem. Geol. 263, 19-36.

Xue, X. Y. and Kanzaki, M., 2004. Dissolution mechanisms of water in depolymerized silicate melts: Constraints from H-1 and Si-29 NMR spectroscopy and ab initio calculations. Geochim. Cosmochim. Ac. 68, 5027-5057.

Yamashita, S., Behrens, H., Schmidt, B. C., and Dupree, R., 2008. Water speciation in sodium silicate glasses based on NIR and NMR spectroscopy. Chem. Geol. 256, 231-241.

https://doi.org/10.5194/se-2019-205
Preprint. Discussion started: 10 January 2020

List of Tables and Figure captions:

Table1. Synthesis conditions and chemical compositions of the $Na_2Si_2O_5$ (NS2) and haplogranite (Hpg) glasses employed as starting materials in this study.

Table 2: Bromine fluid-melt partition coefficients at different P-T conditions. Calculated fluid and melt compositions and densities are also reported.

Table 3. Structural parameters derived from Br K-edge EXAFS analysis for the reference aqueous solutions and silicate glasses at ambient conditions.

Table 4: Br K-edge EXAFS analysis of experimental high P-T fluids with various compositions.

Figure 1. Microphotographs of the compression chamber of the HDAC showing the Haplogranite - H_2O (A, B, C) and NS2 - H_2O (D, E, F) systems at the indicated pressure and temperature conditions. Images are taken through the diamond along the X-ray path. A) Haplogranite glass and 3 wt% NaBr aqueous solution at room conditions; B) globulus of hydrous silicate melt in equilibrium with the aqueous fluid; C) supercritical liquid (single fluid phase); D) NS2 glass and 3 wt% NaBr aqueous solution at room conditions; E) supercritical liquid (low temperature supercriticality); F) hydrous NS2 melt coexisting with aqueous fluid (high temperature subcriticallity).

Figure 2. 2D-SXRF Br K_α intensity maps of Run 1 showing the distribution of Br between coexisting aqueous fluid and haplogranite melt at different P-T conditions. The fluid:glass ratio refers to the wt fraction calculated from the volumetric proportions of loaded glass and sample chamber. The white dashed line delimits the edge of the Re gasket.

Br-enriched phases appear in red and yellow, Br-depleted areas in blue and green. At the beginning of the experiment (A), all the Br is concentrated in the glass. After the glass melts (B), Br strongly partitions into the fluid phase ($D_{Br}^{f/m}$ = 8.07 ±0.79). As temperature increases, the Br concentration in the melt increases while the Br concentrations in the fluid decreases (C). At 821°C - 0.9GPa, the I_f/I_m ratio appears homogeneous as the Br concentrations per volume are almost similar (I_f/I_m = 1.3 ±0.1). However, per weight, Br still partitions preferentially into the fluid ($D_{Br}^{f/m}$ = 2.02 ±0.14).

Figure 3. Evolution of the Br partition coefficients $D_{Br}^{f/m}$ with increasing temperature at different pressure conditions. The different symbols and colors account for separate experimental runs involving different glass proportions. The errors reported on $D_{Br}^{f/m}$ take into account the uncertainties on pressure determination (10%) and on the determination of fluid and melt composition and density from previous studies. The partition coefficients from Bureau et al. (2010) and Cadoux et al. (2018) are shown for comparison. For Cadoux et al., note that both average values from several experiments ($D_{Br}^{f/m}$ = 20.2 ±1.2) and minimum value for a single experiment ($D_{Br}^{f/m}$ = 8.6) are reported.

Figure 4. Normalized Br K-edge XANES spectra collected on Br-bearing silicate glasses, aqueous fluids and hydrous silicate melts at various pressure and temperature conditions. Spectra are offset for clarity. The vertical dashed line is a visual guide to appreciate phase shifts. The black arrow shows the pre-edge feature in the haplogranite glass spectrum corresponding to the 1s to 4p transition in Br (Burattini et al., 1991).

Figure 5. Normalized k^1-weighted EXAFS oscillations of the investigated Br-bearing samples (black solid lines) and corresponding least-square fits (blue dashed lines). Spectra are off-set vertically for clarity. The pressure and temperature conditions and the compositions are reported right to each spectrum.

Figure 6. Evolution of bromine coordination numbers with oxygen (from H_2O molecules) and sodium ($N_{Br\cdots H\text{-}O}$ and $N_{Br\text{-}Na}$) as a function of fluid composition (*i.e*, the weight fraction of NS2 dissolved in the fluid) along the NaBr aqueous solution – NS2 join. The gray field shows the detection limit (DL) for Br-Na complexes, which corresponds to the maximum Br-Na coordination number ($N_{Br\text{-}Na}$) determined for 3wt% NaBr aqueous solution at ambient conditions and 450 °C (DL < 1.5 atoms).

Table 1.

Sample	Synthesis conditions		Br[1] (wt%)	Na_2O[2] (wt%)	SiO_2[2] (wt%)	Al_2O_3[2] (wt%)	K_2O[2] (wt%)	H_2O[3] (wt%)	ASI[4]	Analytical method
	T (°C)	P(GPa)								
NS2-Br1	1200	0.5	4.01	32.0	63.9					EMPA
			4.10							LA-ICPMS
Hpg-Br2	1200	1.5	-	7.1	74.1	9.2	3.7	3.3	0.57	EMPA
			0.96							RBS
Hpg-Br3	1200	1.5	0.89	7.4	75.0	9.4	3.8	3.3	0.57	EMPA

Notes: EMPA = Electron Microprobe Analyses; **LA-ICPMS** = Laser-ablation Inductively Couple Plasma Mass Spectrometry; **RBS** = Rutherford Backscattering Spectroscopy.

[1] Standard deviations (1σ) are 0.04 wt% for RBS analysis, 0.3 wt% for LA-ICPMS and 0.03 wt% for EMPA analysis.

[2] Average from 10 to 25 analyses performed on each glass composition. Standard deviations (1σ) are < 0.1 wt% for Na_2O, Al_2O_3 and K_2O and < 0.3 wt% for SiO_2.

[3] Nominal H_2O concentration (not analyzed).

[4] Aluminum Saturation Index ASI = $\frac{Al_2O_3}{Na_2O+K_2O}$ (in moles).

Table 2.

X_g[1]	T (°C)	P (GPa)[2]	H_2O in melt (wt%)[3]	Melt density ρ_m[4]	Transmission in melt T_m	Silicates in fluid (wt%)[5]	Fluid density ρ_f[7]	Transmission in fluid T_f	I^f_{Br}/I^m_{Br}	$D^{f/m}_{Br}$
Haplogranite – H_2O										
Run 1										
0.76	592	0.7	7.1 ±0.8	2.24	0.66	2.5 ±0.5	0.94	0.96	4.9	**8.1** ±0.8
	694	0.8	7.7 ±0.9	2.23	0.67	5.3 ±1.2	0.97	0.95	2.6	**4.2** ±0.2
	821	0.9	8.0 ±1.0	2.23	0.67	10.3 ±2.3	0.99	0.95	1.3	**2.0** ±0.1
Run 2										
0.82	645	0.9	9.1 ±1.1	2.22	0.67	5.5 ±1.1	1.02	0.95	10.0	**15.3** ±1.0
	710	1.1	11.1 ±1.4	2.20	0.68	11.1 ±2.4	1.09	0.94	5.4	**7.9** ±0.5
	840	0.9	7.9 ±1.0	2.23	0.67	10.8 ±2.4	0.98	0.95	2.8	**4.4** ±0.3
Run 3										
0.72	610	1.2	13.3 ±1.7	2.18	0.69	7.7 ±1.6	1.13	0.95	4.6	**6.4** ±0.3
	730	0.65	6.0 ±0.7	2.25	0.66	3.9 ±0.9	0.88	0.96	2.3	**4.1** ±0.4
	800	0.2	2.4 ±0.2	2.26	0.64	0.7 <0.1	0.49	0.98	1.6	**4.8** ±0.3
Haplogranite – 3 wt% NaBr aqueous solution										
Run 4										
0.70	740	1.7	19.5 ±2.8	2.11	0.72	12.8 ±0.8[6]	1.20	0.94	7.2	**9.7** ±0.6
Error (unless indicated)		±0.1		±0.01	±0.07		±0.04	±0.01	±0.1	

Notes:

[1] Initial weight fraction of glass in the loading.

[2] Maximum uncertainty on pressure were of 10%.

[3] H_2O solubility in the haplogranite melt calculated from the solubility data of Mysen and Wheeler (2000).

[4] Melt density (in g.cm^{-3}) calculated as a function of P-T conditions and melt composition using Malfait et al. (2014).

[5] Solubility of silicate components (SiO_2, Na_2O, Al_2O_3 and K_2O)in the aqueous fluid coexisting with haplogranite melt calculated from the albite solubility data of Anderson and Burnham (1983).

[6] Silicate solubility in the aqueous fluid estimated from Wohlers et al. (2011) for P > 1.2 GPa.

[7] Fluid density (in g.cm^{-3}) calculated as a function of P-T conditions from the data of Mantegazzi et al. (2013)

Table 3.

Composition	**Oxygen (O)**			**Sodium (Na)**			
Aqueous solutions[1]							
	$N_{Br\cdots H\text{-}O}$	$R_{Br\cdots H\text{-}O}$ (Å)	σ^2 (Å^2)				*R-factor*
3 wt% NaBr-H_2O	5.9 ±0.7	3.37 ±0.04	0.02				0.04
2.3 wt% KBr-H_2O.[3]	5.7 ±0.8	3.30 ±0.03	0.02				0.06
Silicate glasses[2]							
	$N_{Br\text{-}O}$	$R_{Br\text{-}O}$ (Å)	σ^2 (Å^2)	$N_{Br\text{-}Na}$	$R_{Br\text{-}Na}$ (Å)	σ^2 (Å^2)	*R-factor*
NS2 glass	5.2 ±2.4	3.45 ±0.09	0.02	5.3 ±1.8	2.99 ±0.09	0.03	0.25
Haplogranite glass	6.1 ±3.6	3.39 ±0.03	0.02	5.9 ±1.8	2.94 ±0.03	0.03	0.21

Notes: N = Br coordination number ($N_{Br\text{-}O}$ or $N_{Br\text{-}Na}$); R = Br-neighbor (Na or O) mean distance (Å); σ^2 = squared Debye-Waller factor (Å^2); *R-factor* = goodness of the fit; $S_0^2 = 1$;

[1] Hydration shell (Br···H-O)

[2] Br coordinated to oxygens from the silicate network (next-nearest coordination shell).

[3] Ferlat et al. (2002), 0.2m KBr-H_2O for comparison.

Table 4.

Composition	**T (°C)**	**P (GPa)**	**$N_{Br\cdots H\text{-}O}$**	**$R_{Br\cdots H\text{-}O}$ (Å)**	**σ^2 (Å^2)**	**$N_{Br\text{-}Na}$**	**$R_{Br\text{-}Na}$ (Å)**	**σ^2 (Å^2)**	***R-factor***
3 wt% NaBr aqueous solution									
	25	0	5.9 ± 0.7	3.37 ±0.04	0.02	bdl[1]			0.04
	320	0.2	6.3 ± 1.8	3.36 ±0.05	0.04	bdl			0.17
	450	0.6	6.4 ±1.1	3.40 ±0.07	0.05	bdl			0.19
Br-bearing aqueous fluids									
1.2 wt% Hpg[3]	475	1	5.4 ±0.9	3.33 ±0.03	0.05	bdl			0.13
5 wt% Hpg	680	0.8	5.7 ±1.1	3.30 ±0.04	0.06	bdl			0.12
0.6 wt% Hpg	750	0.2	5.0 ±1.6	3.33 ±0.06	0.06	bdl			0.30
30 wt% NS2[2]	190	n.d.	6.7 ±1.4	3.38 ±0.03	0.04	bdl			0.14
	320	n.d.	5.7 ±1.4	3.37 ±0.09	0.04	bdl			0.22
50 wt% NS2	580	1.1	4.7 ±1.5	3.35 ±0.15	0.04	bdl			0.25
Br-bearing melt-like fluids									
60 wt% NS2	480	1.5	3.6 ±1.5	3.47 ±0.05	0.01	2.5 ±1.2	3.10 ±0.06	0.01	0.23
	610	2.2	4.8 ±2.4	3.45 ±0.05	0.03	2.6 ±0.9	3.06 ±0.06	0.03	0.20
NS2 melt (10 ±1 wt% H_2O)	710	0.4	3.4 ±1.6	3.36 ±0.03	0.02	6.6 ±2.1	2.91 ±0.03	0.05	0.24

Notes: N = Br coordination number (dissociate as $N_{Br\cdots H\text{-}O}$ and $N_{Br\text{-}Na}$); R = Br-neighbor mean distance (Å); σ^2 = squared Debye-Waller factor (Å^2); *R-factor* = goodness of the fit; $S_0^2 = 1$.

[1] bdl = below detection limit. Detection limit corresponds to the maximum Br-Na coordination number determined for 3 wt% NaBr aqueous solution at ambient conditions.

[2] wt% NS2 indicates the amount of dissolved NS2 in the single phase fluid calculated from the mass of H_2O and NS2 glass.

[3] wt% Hpg refers to the amount of dissolved silicate in the fluid coexisting with haplogranite melt calculated as in Table 3.

Errors in temperature and pressure are ±2 ºC and 10%, respectively. Errors in the composition of the analyzed fluids are within 5% (Table 2).

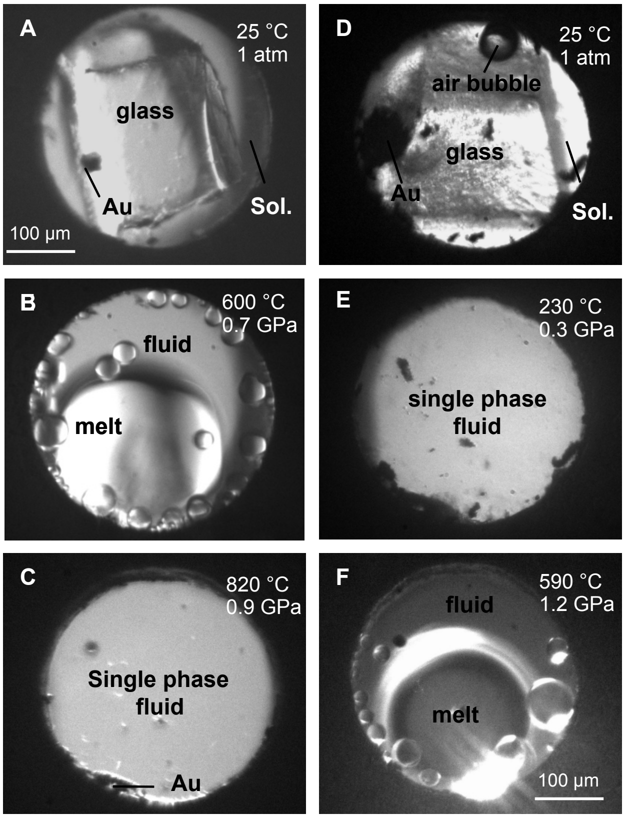
A
25 °C
1 atm
glass
Au
Sol.
100 µm
D
25 °C
1 atm
air bubble
glass
Au
Sol.
B
600 °C
0.7 GPa
fluid
melt
E
230 °C
0.3 GPa
single phase
fluid
C
820 °C
0.9 GPa
Single phase
fluid
Au
F
590 °C
1.2 GPa
fluid
melt
100 µm

Figure 1

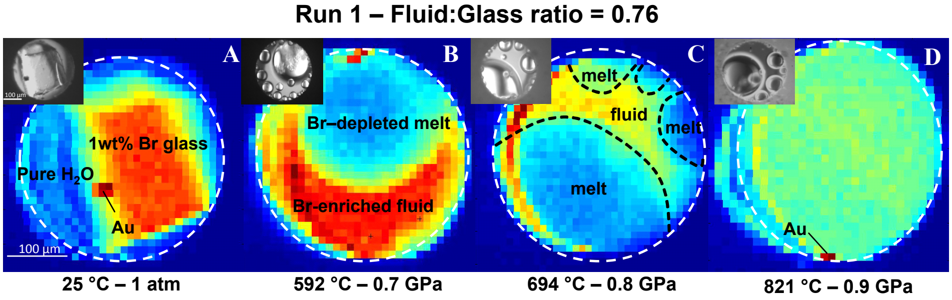
Run 1 – Fluid:Glass ratio = 0.76
A
1wt% Br glass
Pure H_2O
Au
100 µm
B
Br–depleted melt
Br-enriched fluid
C
melt
fluid
melt
melt
D
Au
25 °C – 1 atm
592 °C – 0.7 GPa
694 °C – 0.8 GPa
821 °C – 0.9 GPa

Figure 2

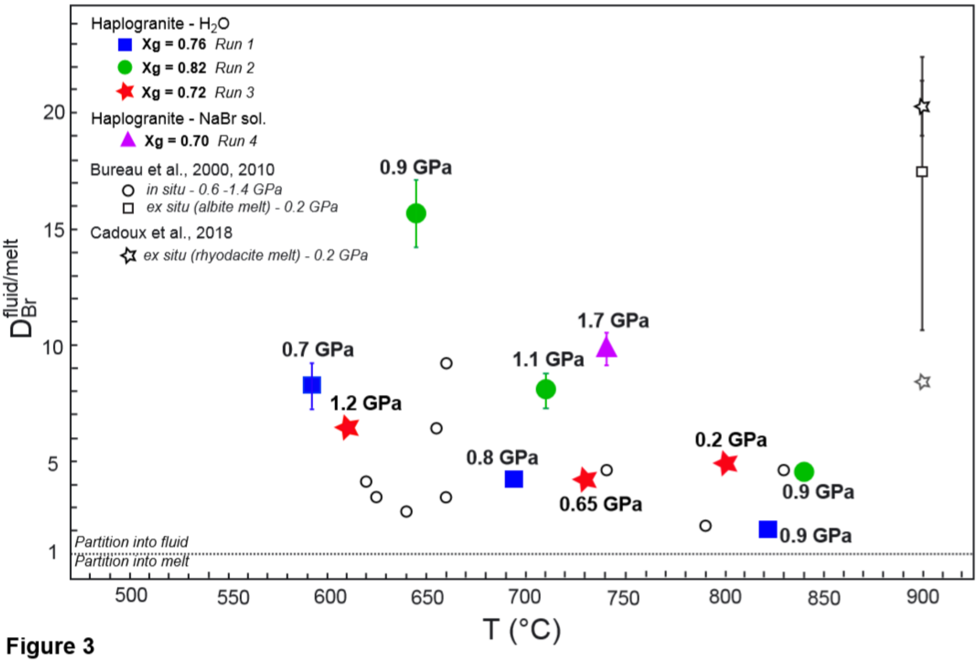
Haplogranite - H_2O
Xg = 0.76 Run 1
Xg = 0.82 Run 2
Xg = 0.72 Run 3
Haplogranite - NaBr sol.
Xg = 0.70 Run 4
Bureau et al., 2000, 2010
in situ - 0.6 -1.4 GPa
ex situ (albite melt) - 0.2 GPa
Cadoux et al., 2018
ex situ (rhyodacite melt) - 0.2 GPa
$D_{Br}^{fluid/melt}$
T (°C)
0.9 GPa
0.7 GPa
1.2 GPa
1.1 GPa
1.7 GPa
0.8 GPa
0.65 GPa
0.2 GPa
0.9 GPa
0.9 GPa
Partition into fluid
Partition into melt
1
5
10
15
20
500
550
600
650
700
750
800
850
900

Figure 3

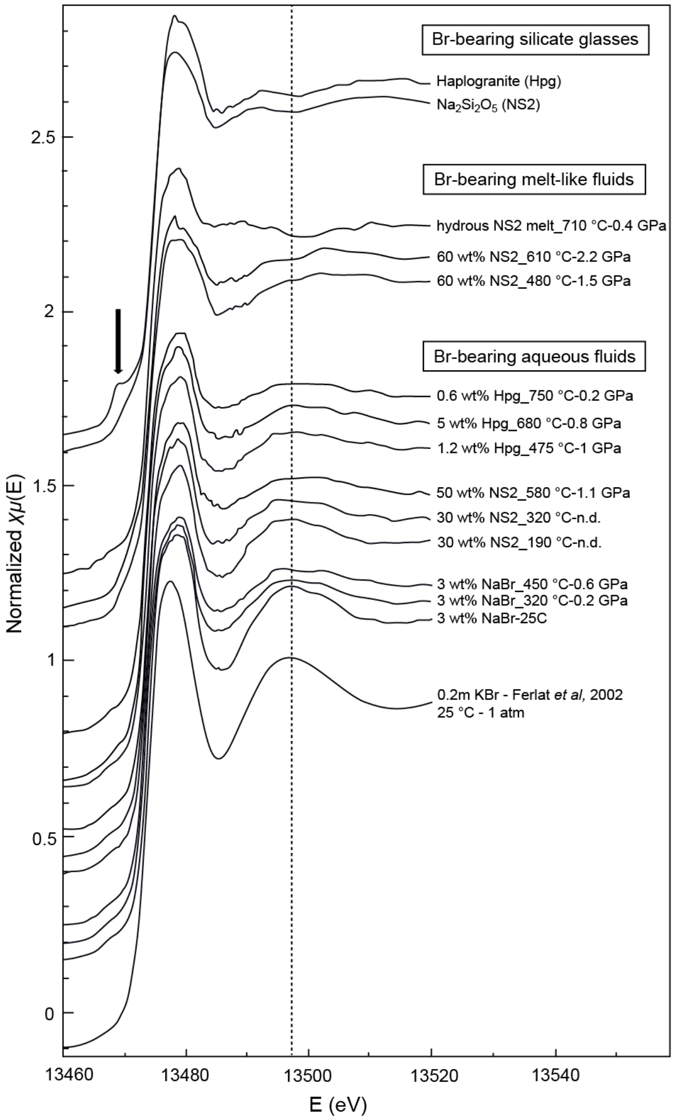
Br-bearing silicate glasses
Haplogranite (Hpg)
$Na_2Si_2O_5$ (NS2)
Br-bearing melt-like fluids
hydrous NS2 melt_710 °C-0.4 GPa
60 wt% NS2_610 °C-2.2 GPa
60 wt% NS2_480 °C-1.5 GPa
Br-bearing aqueous fluids
0.6 wt% Hpg_750 °C-0.2 GPa
5 wt% Hpg_680 °C-0.8 GPa
1.2 wt% Hpg_475 °C-1 GPa
50 wt% NS2_580 °C-1.1 GPa
30 wt% NS2_320 °C-n.d.
30 wt% NS2_190 °C-n.d.
3 wt% NaBr_450 °C-0.6 GPa
3 wt% NaBr_320 °C-0.2 GPa
3 wt% NaBr-25C
0.2m KBr - Ferlat *et al*, 2002
25 °C - 1 atm
Normalized xμ(E)
2.5
2
1.5
1
0.5
0
13460
13480
13500
13520
13540
E (eV)

Figure 4

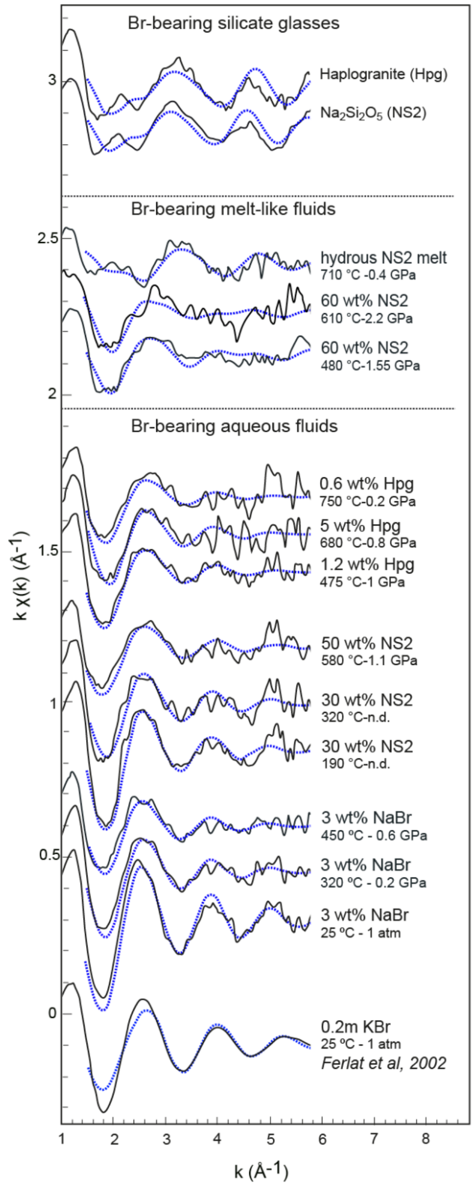
Br-bearing silicate glasses
Haplogranite (Hpg)
$Na_2Si_2O_5$ (NS2)
Br-bearing melt-like fluids
hydrous NS2 melt
710 °C -0.4 GPa
60 wt% NS2
610 °C-2.2 GPa
60 wt% NS2
480 °C-1.55 GPa
Br-bearing aqueous fluids
0.6 wt% Hpg
750 °C-0.2 GPa
5 wt% Hpg
680 °C-0.8 GPa
1.2 wt% Hpg
475 °C-1 GPa
50 wt% NS2
580 °C-1.1 GPa
30 wt% NS2
320 °C-n.d.
30 wt% NS2
190 °C-n.d.
3 wt% NaBr
450 ºC - 0.6 GPa
3 wt% NaBr
320 ºC - 0.2 GPa
3 wt% NaBr
25 ºC - 1 atm
0.2m KBr
25 ºC - 1 atm
Ferlat et al, 2002
k χ(k) (Å-1)
3
2.5
2
1.5
1
0.5
0
1
2
3
4
5
6
7
8
k (Å-1)

Figure 5

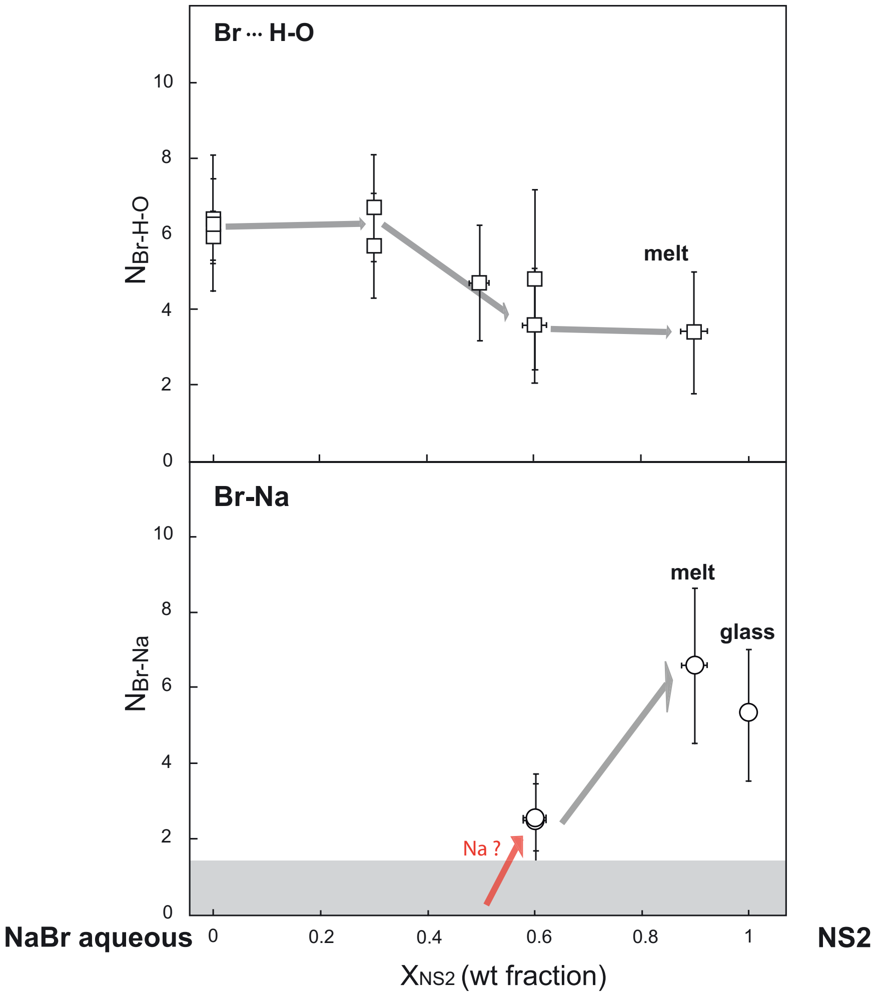

937

938

939 **Figure 6**